INTERNATIONAL JOURNAL FOR NUMERICAL METHODS IN FLUIDS
Int. J. Numer. Meth. Fluids 2003; **41**:1021–1051 (DOI: 10.1002/fld.476)

Three-dimensional transient free-surface flow of viscous fluids inside cavities of arbitrary shape

Kyu-Tae Kim and Roger E. Khayat*,†

Department of Mechanical and Materials Engineering, The University of Western Ontario, London, Ont., Canada N6A 5B9

SUMMARY

The three-dimensional transient free-surface flow inside cavities of arbitrary shape is examined in this study. An adaptive (Lagrangian) boundary-element approach is proposed for the general three-dimensional simulation of confined free-surface flow of viscous incompressible fluids. The method is stable as it includes remeshing capabilities of the deforming free-surface, and thus can handle large deformations. A simple algorithm is developed for mesh refinement of the deforming free-surface mesh. Smooth transition between large and small elements is achieved without significant degradation of the aspect ratio of the elements in the mesh. The method is used to determine the flow field and free-surface evolution inside cubic, rectangular and cylindrical containers. These problems illustrate the transient nature of the flow during the mixing process. Surface tension effects are also explored. Copyright © 2003 John Wiley & Sons, Ltd.

KEY WORDS: free-surface flow; cavity flow; viscous flow

1. INTRODUCTION

The flow inside a cavity is of direct relevance to mixing, in particular lid-driven cavity flow. Besides its fundamental importance, this flow has been often examined as a benchmark problem for laminar and turbulent flows to test proposed numerical simulation schemes. However, almost all problems solved were limited to confined two-dimensional steady flow. Only a few have tackled the three-dimensional flow using direct numerical simulation [1–5], and analytical techniques for Stokes flow only [6, 7]. In this study, the Stokes flow field is determined in the presence of a free surface, as typically encountered in open mixers. The study focuses on the transient response after inception. In particular, the evolution of the free surface will be monitored as the surface deforms under the action of flow.

* Correspondence to: R. E. Khayat, Department of Mechanical & Materials Engineering, The University of Western Ontario, London, Ontario, Canada N6A 5B9.
† E-mail: rkhayat@eng.uwo.ca

Contract/grant sponsor: Natural Sciences and Engineering Research Council of Canada

Received June 2001
Revised 30 July 2002

The numerical simulation of transient free-surface flow problems remains challenging despite the advent of powerful techniques. Several numerical techniques have been developed for the solution of moving boundary/initial value problems. These techniques may be classified as Eulerian, Lagrangian and mixed Eulerian–Lagrangian [8]. In the Eulerian description of the flow, the grid points remain stationary or move in a predetermined manner [9–12]. Typically, the fluid moves in and out of the computational cells. The method can handle arbitrarily large free-surface deformations without loss of accuracy. Its main disadvantage, however, is the lack of sharp definition of the free surface, and the consequent difficulty to impose the kinematic and dynamic boundary conditions on the free surface. In the Lagrangian approach, the grid points move with local fluid particle [13, 14]. The free surface is sharply defined and it is easy to impose the necessary boundary conditions. However, Lagrangian methods require mesh refinement or remeshing for large deformations of the free surface. Hybrid methods have also been developed that combine the advantages of the Eulerian and Lagrangian methods [15]. Generally, an adaptive Lagrangian approach becomes difficult to implement when a volume method such as the finite-element method (FEM) is used. On the other hand, the boundary-element method (BEM) is much easier to use along with adaptive remeshing as the dimension of the problem is reduced by one.

The BEM relates velocities at points within the fluid to the velocity and stress on the bounding surfaces. It is thus an ideal method for studying moving-boundary problems where the velocity on the free surface is the quantity of prime interest. The advantages of the BEM include: reduction of problem dimensionality, direct calculation of the interfacial velocity, the ability to track large surface deformations, and the potential for easy incorporation of interfacial tension as well as other surface effects. The BEM has recently been applied to a variety of problems of the moving-boundary type. Such problems include the deformation of a drop in a confined medium [16–21], conventional and gas-assisted injection molding [22, 23], air venting during blow molding and thermoforming [24], and the transient mixing of Newtonian and viscoelastic fluids [25, 26]. The present work addresses the numerical solution of a class of moving-boundary problems in a confined medium of the free-surface type. An adaptive Lagrangian boundary-element approach is adopted to determine the evolution of the free surface. The formulation and numerical implementation are illustrated for a flow advancing inside and exiting a confining cavity.

A simple algorithm for adaptive refinement of the (two-dimensional) triangular mesh of the free surface is implemented. A number of algorithms for adaptive generation of triangular meshes have been proposed before. Some methods generate entirely new meshes [27, 28], others subdivide elements of an initial mesh [29, 30], and still others can both generate new meshes and subdivide the meshes adaptively [31]. A comprehensive survey of automatic mesh generation algorithms is given by Sheppard [32]. In the present study, the initial mesh is assumed to be regular so that no initial mesh refinement is needed. As the free surface evolves with time, the triangular elements grow and become distorted. Beyond a prescribed level of distortion, an element is subdivided into two elements. Additional nodes are added only at the mid-side of the longest edge of the element. This method ensures the preservation of a good aspect ratio for the elements in the mesh. Rivara has implemented this method [30], but his procedure requires a search process to repair any incompatibilities that may be generated. Dow and Byrd also employed this approach in the refinement of regions with simple rectangular boundaries [33].

The paper is organized as follows. The problem formulation is presented in Section 2, where basic equations and boundary conditions are covered. The solution procedure, including the time-marching scheme, adaptive meshing of the free surface, determination of local curvature, and the contact problem are discussed in Section 3. Numerical assessment and results are covered in Section 4. Finally, some concluding remarks are given in Section 5.

2. PROBLEM FORMULATION

In this section, the governing equations, domain description and boundary conditions are reviewed together with some of the assumptions taken for the moving-boundary flow of viscous incompressible Newtonian fluids. Only low-Reynolds-number flows, typically characterized by small velocities, small length scales and/or high viscosity, will be considered. In this limit, the inertia terms in the momentum equation are negligible, so the flow is in a state of creeping motion. The formulation is thus limited to Stokes flow.

2.1. Governing equations

Consider the flow of a fluid of density ρ, viscosity μ, and surface tension coefficient γ. At any instant, t, the fluid is assumed to occupy a three-dimensional region, $\Omega(t)$, which is bounded by $\Gamma(t)$. It is convenient to take $\Omega(t)$ as the inner domain, excluding $\Gamma(t)$. Thus, $\Omega(t) \cup \Gamma(t)$ constitutes the domain occupied by the fluid. The fluid is taken to be neutrally buoyant so the effects of gravity and any external body forces are negligible. The conservation of mass and linear momentum equations are given by

$$\nabla \cdot \mathbf{u}(\mathbf{x},t) = 0, \quad \nabla \cdot \sigma(\mathbf{x},t) = \mathbf{0}, \quad \mathbf{x} \in \Omega(t) \cup \Gamma(t) \tag{1}$$

where ∇ is the gradient operator, $\mathbf{x}$ is the position vector, $\mathbf{u}(\mathbf{x},t)$ is the velocity vector, and $\sigma(\mathbf{x},t)$ is the total stress tensor given in terms of the hydrostatic pressure $p(\mathbf{x},t)$ and excess stress tensor $\tau(\mathbf{x},t)$. Here $\sigma(\mathbf{x},t) = -\,p(\mathbf{x},t)\mathbf{I} + \tau(\mathbf{x},t)$, where $\mathbf{I}$ is the identity tensor. In the present study, the fluid is assumed to be Newtonian, so that

$$\tau(\mathbf{x},t) = \mu\lfloor \nabla\mathbf{u}(\mathbf{x},t) + \nabla\mathbf{u}^{\mathrm{T}}(\mathbf{x},t)\rfloor \quad \mathbf{x} \in \Omega(t) \cup \Gamma(t) \tag{2}$$

where μ is the viscosity of the fluid. The superscript T denotes the transpose of the matrix. It is important to note that the acceleration term $\partial\mathbf{u}/\partial t$ in the momentum conservation equation has been neglected, so that for a Newtonian fluid, the formulation in question is not strictly unsteady, but quasi-steady. This quasi-steady state assumption is valid whenever $L^2/v \ll T$, where L and T are typical characteristic length and time of the flow, and $v = \mu/\rho$ is the kinematic viscosity (ρ being the density). In the case of cavity flow, $T \sim L/U$, U being a typical value of the driving velocity. Thus, for the quasi-steady state assumption to apply, one must have $UL/v \ll 1$. This is indeed typically the case for fluids of interest to mixing. Note also that this inequality is implied by the smallness of the Reynolds number. Physically, the quasi-steady state approximation means that a Newtonian fluid immediately adjusts to changes in the movement of the boundary or boundary conditions.

2.2. Domain of computation of the free-surface-flow problem

There are various classes of free-surface flow problems that can be considered by the proposed formulation, with direct relevance to polymer processing. Most notable examples are conven-

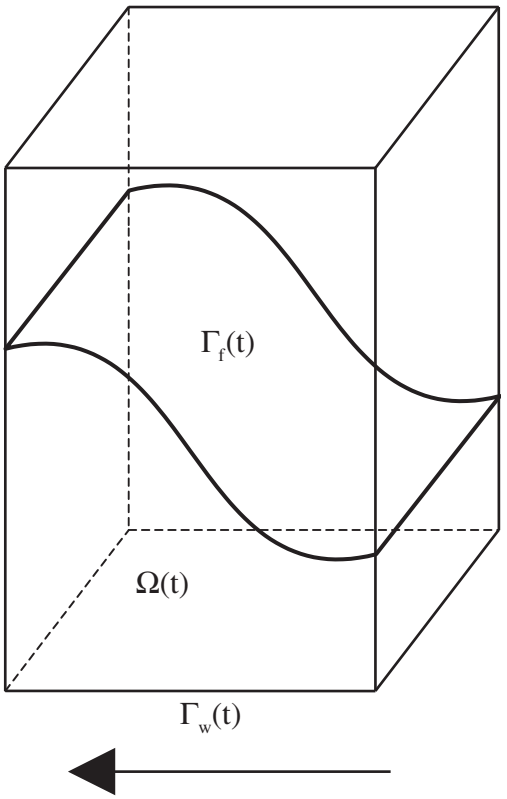

Figure 1. Schematic illustration of transient free-surface flow inside a cavity of arbitrary shape.

tional and gas-assisted injection molding, coating, extrusion, thermoforming, blow molding and mixing. These problems may be conveniently divided into two categories: continuous and discrete flows. A continuous flow involves the growth of a domain as a result of an extended influx of fluid over a period of time, such as during injection molding and extrusion. In contrast, a discrete flow is induced by the action of an external force, usually pressure or the velocity at the boundary, which acts on a given and constant amount of fluid, such as during gas-assisted injection molding, thermoforming, blow molding and mixing. Figure 1 illustrates typically the mixing process inside a partially filled cavity of arbitrary shape. In this case, the flow is assumed induced by the translation of part of the boundary. The boundary, $\Gamma(t)$, in Figure 1 is composed, at any time, of the wetted part of the cavity, $\Gamma_w(t)$, and the moving free surface, $\Gamma_f(t)$. The wetted part of the cavity depends on time since it changes with the movement of the fluid that is in contact with the wall. The overall boundary may thus be expressed as $\Gamma(t) = \Gamma_w(t) \cup \Gamma_f(t)$.

2.3. Boundary and initial conditions

The velocity is assumed to be fully prescribed on the wetted part of the boundary. In this study, and as indicated in Figure 1, the flow is assumed to be induced by the steady movement

of the lower part of $\Gamma_w(t)$. The fluid is assumed to adhere to the cavity boundary, so that stick and no-penetration boundary conditions apply on the wetted part of the cavity. Generally, one has

$$\mathbf{u}(\mathbf{x},t)=\mathbf{u}_w(\mathbf{x}),\quad \mathbf{x}\in\Gamma_w(t) \tag{3}$$

where $\mathbf{u}_w(\mathbf{x})$ is zero at the stationary parts of $\Gamma_w(t)$.

The dynamic condition on the free surface is based on the continuity of the tangential stress and discontinuity of normal stress caused by the interfacial tension:

$$\mathbf{t}(\mathbf{x},t)=\gamma\mathbf{n}(\mathbf{x},t)\nabla\cdot\mathbf{n}(\mathbf{x},t),\quad \mathbf{x}\in\Gamma_f(t) \tag{4}$$

Here $\mathbf{t}(\mathbf{x},t)=\boldsymbol{\sigma}(\mathbf{x},t)\cdot\mathbf{n}(\mathbf{x},t)$ is the traction, $\mathbf{n}$ is the normal unit vector at $\Gamma_f(t)$. Note that boundary condition (4) is derived under conditions of equilibrium and uniform interfacial tension. Its validity under dynamic conditions is simply assumed [34, 35]. The condition also assumes implicitly that the flow activity of the fluid outside the moving boundary (air) is negligible with the (atmospheric) pressure taken as zero.

The proper choice and implementation of a kinematic condition is generally not obvious, especially from a numerical standpoint [8]. This condition relates the evolution of the moving boundary to the local velocity field. The moving boundary deforms in accord with the instantaneous velocity field, thus determining new moving boundary positions with time. In the present Lagrangian representation, the moving boundary may be assumed to deform with the fluid velocity, such that the evolution of $\Gamma_f(t)$ is governed by the equation

$$\frac{d\mathbf{x}}{dt}=\mathbf{u}(\mathbf{x},t),\quad \mathbf{x}\in\Gamma_f(t) \tag{5}$$

Although easy to implement, the resulting scheme based on Equation (5) tends to sweep points on the moving boundary along the tangent to the moving boundary, even if only small shape changes take place. Consequently, frequent redistribution of the moving boundary points or remeshing becomes necessary. Alternatively, the moving boundary can be assumed to deform pointwise along the normal with the normal projection of the fluid velocity at the moving boundary [8]. This method keeps the points evenly distributed on the moving boundary. Thus, the following kinematic boundary condition results:

$$\frac{d\mathbf{x}}{dt}=\mathbf{n}(\mathbf{x},t)[\mathbf{n}(\mathbf{x},t)\cdot\mathbf{u}(\mathbf{x},t)],\quad \mathbf{x}\in\Gamma_f(t) \tag{6}$$

Unlike Equation (5), the above equation prevents the nodes to be swept along the tangent to the moving boundary. However, it leads to numerical instability of the saw-tooth type. This difficulty is usually circumvented by applying a smoothing technique of the discretized surface. Given the remeshing capabilities of the present approach, the use of Equation (6) turned out to be the good choice for the class of problems covered in this study.

As to the initial conditions, the fluid is assumed to be at rest initially, and the following condition is used:

$$\mathbf{u}(\mathbf{x},t=0)\equiv\mathbf{0},\quad \mathbf{x}\in\Omega(t=0)\cup\Gamma(t=0) \tag{7}$$

Thus, the flow field is determined through the solution of Equations (1) and (2) subject to initial condition (7) and the boundary conditions above, using the boundary-integral method.

2.4. Boundary integral equation

The general time-dependent integral equation for a moving domain is given by [36]:

$$\int_{\Gamma(t)} \mathbf{t}(\mathbf{y},t)\cdot\mathbf{J}(\mathbf{x}|\mathbf{y})\,d\Gamma_y - \int_{\Gamma(t)} \mathbf{n}(\mathbf{y},t)\cdot\mathbf{u}(\mathbf{y},t)\cdot\mathbf{K}(\mathbf{x}|\mathbf{y})\,d\Gamma_y = c(\mathbf{x},t)\cdot\mathbf{u}(\mathbf{x},t), \quad \mathbf{x}\in\Omega(t)\cup\Gamma(t) \tag{8}$$

Here $\mathbf{J}$ and $\mathbf{K}$ are the usual symmetric and anti-symmetric tensors with respect to $\mathbf{r}=\mathbf{x}-\mathbf{y}$, and are given as [36]:

$$\mathbf{J}(\mathbf{x}|\mathbf{y}) = -\frac{1}{8\pi}\left(\frac{\mathbf{I}}{r}+\frac{\mathbf{rr}}{r^3}\right), \quad \mathbf{K}(\mathbf{x}|\mathbf{y}) = -\frac{3}{4p}\frac{\mathbf{rrr}}{r^5} \tag{9}$$

where $r=|\mathbf{r}|$. The function $c(\mathbf{x},t)$, for $\mathbf{x}\in\Gamma(t)$, depends on the geometrical form of the boundary; its value arises from the jump in the value of the velocity integrals as the boundary is crossed. Note that $c(\mathbf{x},t)=0$ for $\mathbf{x}\in\Omega(t)$. When the boundary is Lyapunov smooth, which requires that a local tangent to the free surface exists everywhere, the function $c(\mathbf{x},t)=\frac{1}{2}$. This is the case if constant boundary elements are used. Thus, the assumption of boundary smoothness is generally not valid in the vicinity of sharp corners, cusps or edges. In general, since $c(\mathbf{x},t)$ depends solely on geometry, it may be evaluated assuming that a uniform velocity field such as $\mathbf{u}(\mathbf{x},t)=u\mathbf{e}$ is applied over the boundary, $\mathbf{e}$ being the direction of the velocity and u is its magnitude. Under these conditions, all derivatives (including tractions and stresses) must vanish. Hence, at any time t, Equation (8) reduces to

$$c(\mathbf{x},t) = -\int_{\Gamma(t)} \mathbf{n}(\mathbf{y},t)\cdot[\mathbf{e}\cdot\mathbf{K}(\mathbf{x}|\mathbf{y})\cdot\mathbf{e}]\,d\Gamma_y, \quad \mathbf{x}\in\Gamma(t) \tag{10}$$

Thus, at any time t, the form of the boundary $\Gamma(t)$ is determined, and the function $c(\mathbf{x},t)$ is evaluated using the equation above.

3. SOLUTION PROCEDURE

In this section, a time-marching scheme is proposed to discretize Equation (6). Once the flow field is determined at a given time step from Equation (8), the location of the moving boundary can be determined by solving Equation (6). As the boundary elements are distorted, the mesh is refined through element subdivision. The problem of contact between evolving moving boundary and surrounding cavity walls is finally discussed.

3.1. Time-marching scheme and moving boundary evolution

Consider now the application of the integral Equation (8) for a point on the boundary, that is, for $\mathbf{x}\in\Gamma(t)$. The flow field at any interior point $\mathbf{x}\in\Omega(t)$ is obtained once the velocity and traction at the boundary are known. Since the velocity is fully prescribed on $\Gamma_w(t)$, only the traction (or stress) will be determined there. The traction is imposed on the moving boundary, $\Gamma_f(t)$, where the value of the velocity will be found. More explicitly, Equation (8) may be

rewritten as

$$\int_{\Gamma_w(t)} \mathbf{t}(\mathbf{y},t)\cdot\mathbf{J}(\mathbf{x}|\mathbf{y})\,d\Gamma_y - \int_{\Gamma_f(t)} \mathbf{u}(\mathbf{y},t)\cdot[\mathbf{n}(\mathbf{y},t)\cdot\mathbf{K}(\mathbf{x}|\mathbf{y})]\,d\Gamma_y$$
$$+\gamma\int_{\Gamma_f(t)} [\mathbf{n}(\mathbf{y},t)\nabla\cdot\mathbf{n}(\mathbf{y},t)]\cdot\mathbf{J}(\mathbf{x}|\mathbf{y})\,d\Gamma_y + \int_{\Gamma_w(t)} \mathbf{u}_w(\mathbf{y})\cdot[\mathbf{n}(\mathbf{y})\cdot\mathbf{K}(\mathbf{x}|\mathbf{y})]\,d\Gamma_y$$
$$= \begin{cases} c(\mathbf{x},t)\mathbf{u}_w(\mathbf{x}), & \mathbf{x}\in\Gamma_w(t) \\ c(\mathbf{x},t)\mathbf{u}(\mathbf{x},t), & \mathbf{x}\in\Gamma_f(t) \end{cases} \tag{11}$$

where conditions (3) and (4) are used. The unknowns in Equation (11) are thus $\mathbf{t}(\mathbf{x}\in\Gamma_w,t)$ and $\mathbf{u}(\mathbf{x}\in\Gamma_f,t)$, so that the values of the third and fourth integrals on the left-hand side are known.

The time derivative in Equation (6) is approximated by an explicit Eulerian finite-difference scheme, with higher-order terms in the time increment, Δt, being neglected. The integral Equation (11) relates the velocity and traction at the current time. Once the flow field is determined at each time step, t, the position of the moving boundary is updated. The evolution of $\Gamma_f(t)$ is dictated by Equation (6). The updated position of the nodes that belong to the moving boundary is thus determined once the velocity at the moving boundary is obtained from the solution of Equation (11).

The integrals in Equation (11) are discretized into a finite sum of contributing terms over the boundaries. In this work, the boundary elements are assumed to be geometrically linear so that the velocity and traction are constant over each element. This makes the proposed adaptive remeshing method and estimation of curvature less difficult to implement since no interpolation of the flow variables is needed at each time step. The use of higher-order elements is possible, but may not be crucial given the mesh refinement and remeshing capabilities involved in the current procedure. The traction is constant over flat linear element, and is multiply valued at a corner node if higher-order elements are used. In two dimensions, the traction may be assumed to be double valued at every node of a curved boundary. Another advantage of the constant boundary element is that the value of $c(\mathbf{x},t)$ is always and everywhere equal to $1/2$. In addition, the normal vector to each element is determined exactly.

3.2. Adaptive meshing

A simple algorithm is proposed for adaptive refinement of the triangular mesh of the evolving free surface. The method is similar to that proposed by Nambiar *et al.* [37] for adaptive and h refinement of 2D triangular finite-element meshes. Initially ($t<0$), the fluid is assumed to occupy a 3D region, $\Omega_0=\Omega(t=0)$, bounded by the cavity walls and free surface. Typically, at $t\geqslant 0$, some elements become too distorted, and mesh refinement or remeshing is needed as a result of surface deformation. The refinement is carried out by subdividing the elements that are too distorted. Generally, the criteria for subdivision are based on the element area and the length of the edges. However, it turns out that the length of the longest edge is a reliable criterion by itself. In this case, at each time step of the flow, a list of elements is established, with the length of the longest edge greater than an imposed tolerance, $D_{\max}$. The list is sorted in the order of increasing length of the longest edges of each element. In order to avoid generating mesh incompatibilities or elements with poor aspect ratio during refinement,

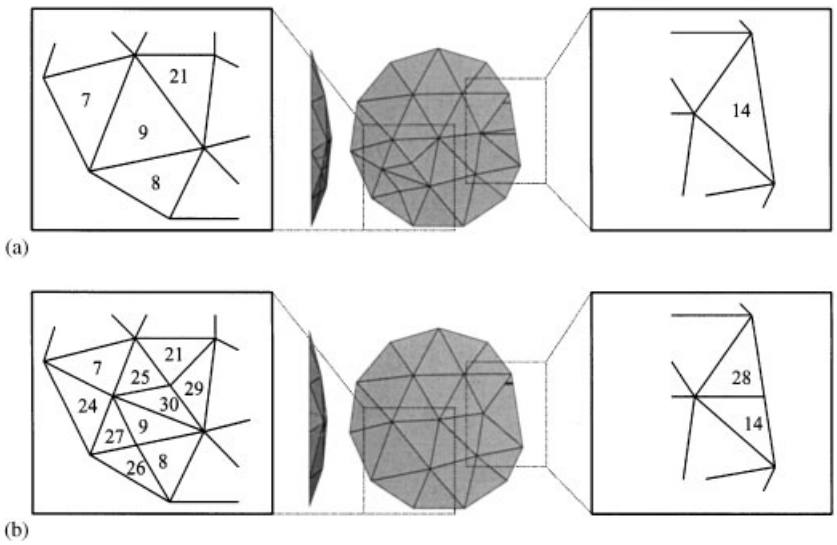

Figure 2. Adaptive meshing and subdivision of free-surface elements. The figure shows the subdivision of a typical internal element (a), and an element on the edge (b).

larger elements are subdivided first. The subdivision starts from the last (i.e. the longest edge) element in the list, and is continued recursively until the list is empty. The subdivision is carried out by bisecting the largest of the edges of the element in the list.

Two distinct cases of element subdivision arise, which are illustrated in Figure 2. The figure displays the subdivision process for a 3D surface that has expanded. In the first case (Figure 2(a)), an element inside the domain (e.g. elements 9 and 21) is subdivided, and in the second case (Figure 2(b)), the element has an edge on the boundary of the domain (element 14). In the latter case, the subdivision process is straightforward. Once the subdivision criteria are reached, the element is simply subdivided into two elements. This is typically illustrated in Figure 2(b) for element 14, which is subdivided into elements 14 and 28. In the former case, the edge of the element is in the interior, and additional options must be considered. To prevent creation of any non-conforming interior elements, the element that shares the common longest edge is also bisected along with the first element. Creation of four elements in such a manner is carried out only when the bisected edge is the longest edge of both elements. If this condition is not met, the second element is added to the end of the element list, which contains the distorted elements so that the second element is now the current element for subdivision and the process is repeated. Again, the element selected for subdivision will have an edge that is the longest among the edges of the elements in the list.

In order to facilitate the search for the second element and the longest edge of elements, the input data are initially processed to create three data structures, one structure for the nodes, one for the triangles and one for the edges. A node is defined by its x-, y- and z-co-ordinate. The properties selected for a triangle are its three nodes, A, B and C, its three edges, AB, BC and CA, and its area. The above information is structured such that the node numbers are ordered in counterclockwise direction for each element and edge AB is the longest edge of

each element. The properties of an edge are its two end nodes, its two neighbouring triangles, and the length of the edge.

The major advantage of dividing only the largest edge in a triangle is that the smallest angle in the original mesh is not further subdivided. If the largest angle C is greater than 90°, none of the newly created angles can be smaller than the original smallest angle A. If C is equal to 90°, the smallest angle A is duplicated as D. If, however, C is smaller than 90°, the newly created angle D is slightly smaller than A. Further, if an angle A is smaller than 60°, it will never be bisected using this algorithm. Rosenberg and Stenger have shown that the smallest angle that can be created in any subsequent mesh produced by the above method is bounded by half the minimum angle present in the initial mesh [38]. Thus, the aspect ratio of the triangles in the mesh remains in an acceptable and known range. The process of subdivision shown in Figure 2(a) illustrates the general sequence of mesh refinement. Elements 7 and 9 are first subdivided each into two triangles; element 7 is now divided into the current elements 7 and 24, while element 9 is divided into one triangle composed currently of 25 and 30, and another composed of currently elements 9 and 27. Subsequently, element 21 is subdivided into elements 21 and 29, along with element composed currently of 25 and 30. Similarly, element 8 is divided into elements 8 and 26, along with the element composed currently of 9 and 27.

The first step in the solution procedure consists then of creating first the data file containing the description of the problem domain, boundary conditions, loading and initial mesh. The initial mesh is first examined to check for initially distorted elements. This mesh comes from a CAD system, such as PATRAN or PROENGINEER. The initial mesh is then refined by the adaptive remeshing scheme described above. The refined mesh is then submitted to the BEM solver. In practice it is found that the quality of the initial mesh is adequate, and any initial refinement is not deemed necessary. This is the case, for instance, of the mesh in Figure 2 before subdivision.

3.3. Determination of local curvature

The value of the curvature at a particular location (node or element) on the free surface is needed if surface tension is accounted for. The curvature is obviously related to the divergence of the normal vector, $\mathbf{n}(x, y, z, t)$, at the location in question. Thus, the determination of the curvature is based on the estimation of the derivative of the normal vector components in the three directions. For this, it is convenient to define local coordinates (ξ, η, n) spanned by the plane tangent to the surface at the local point and the normal to the plane.

Consider now the curvature at an element (centroid) of the discretized surface. The curvature is estimated directly at the centroid of the element rather than on a smooth interpolated surface going through the element vertices. Surface interpolation and fitting can be very costly. Generally, each node of the triangle belongs to an arbitrary number of elements, and the normal at the node is not uniquely defined. The normal vector is then taken as the area average of the normal vectors to the elements to which the node belongs. The normal vector anywhere to the element, with vertices 1, 2 and 3, may then be generally written as

$$\mathbf{n}(\mathbf{x}, t) = \sum_{i=1}^{3} \mathbf{n}_i(t)\phi_i[\xi(\mathbf{x}, t), \eta(\mathbf{x}, t)] \tag{12}$$

where $\mathbf{n}_i(t)$ are the normal vectors at node i, and $\phi_i(\mathbf{x},t)$ are suitably introduced interpolation functions. In this work, given the fact that flat triangular elements are used, $\phi_i(\mathbf{x},t)$ are taken to be linear. The partial derivatives of the normal vector are obtained by differentiating Equation (12). If the (ξ,η) co-ordinate axes are taken to lie in the plane of the element, then:

$$\nabla \cdot \mathbf{n} = \frac{\partial n_\xi}{\partial \xi} + \frac{\partial n_\eta}{\partial \eta} \tag{13}$$

and the curvature is just given by $-\nabla \cdot \mathbf{n}/2$. This procedure is now validated by computing the curvature for simple surfaces, discretized in triangular flat elements. Two examples are treated, namely, the case of a spherical shell of radius equal to one, and the case of a parabolic surface.

3.3.1. Case of a spherical surface. Two mesh sizes are considered for the sphere of radius one. The first mesh consists of 72 elements and 38 nodes, and the second of 272 elements and 138 nodes. The curvature, in this case, with the normal vector pointing outward, is equal to -1. The computed curvature for the sphere composed of 72 elements lies within the interval $[-0.912,\ -0.885]$. The average value of the curvature is equal to -0.903, which corresponds to a global error of 9.7%. For this mesh, the small dispersion in the numerical values of the curvature indicates that the uniformity in the mesh is preserved. The curvature is computed at the centroid of the elements. Given the construction of the mesh, which places the nodes on a sphere of radius one, the centroids do not coincide exactly with the sphere. The deviation in position between the centroids of the elements and the corresponding position on the sphere is typically equal to 8%. This value is of the same order of magnitude as the error in the estimation of the curvature. The results of the numerical computation of the curvature for this mesh are thus conclusive. The uniformity of the entire mesh is preserved, and the resulting error corresponds to that of the mesh size. This consistency is not always achieved for any mesh as the next case shows.

The influence of mesh size on the computed curvature is examined by considering the mesh of 272 elements. In this case, the computed average curvature is found to be closer to -1, namely, -0.95. However, the difference between the maximum and the minimum values is larger. The former is equal (in magnitude) to -1.25 and the latter is equal to -0.68. These extreme values correspond to regions where the elements are not regular. A curvature can have a magnitude that is too small, for instance, two or more elements happen to lie almost in the same plane. The opposite is true when, for instance, the planes of two elements make an angle of less than 90°. These mesh irregularities do indeed happen and there is little that can be done to control them. Localized errors can be large, exceeding 30% for a couple of nodes in the present example. However, if the couple of irregular points are excluded, the average error in the computed curvature is only 3%, which also corresponds to the error in the location of the centroids of the elements relative to a sphere of radius one.

This second mesh confirms that a good estimate of the curvature depends on two major factors: mesh size and regularity. Obviously, a finer mesh leads globally to an accurate estimate of the curvature. However, strong irregularity results in large errors locally. The accuracy of the current method hinges on the accuracy of the normal vectors at the nodes and (their average) over each element. It is thus essential to start with an optimized original mesh.

Indeed, four mesh sizes are examined that help establish the convergence rate with mesh refinement. The meshes are generated with reasonable regularity. The mesh sizes considered

Table I. Influence of mesh size on the accuracy in estimating the curvature for a sphere.

No. of elements	Relative error	Standard deviation
192	0.0302	0.0291
312	0.0175	0.0170
406	0.0148	0.0145
600	0.0125	0.0123

Table II. Influence of mesh size on the accuracy in estimating the curvature for a parabolic surface.

No. of elements	Relative error	Standard deviation
100	0.524	1.910
400	0.180	0.213
900	0.097	0.090
2500	0.046	0.044

correspond to 192, 312, 406 and 600 elements. The resulting average relative error and standard deviation for each mesh size are reported in Table I. The error and standard deviation decrease with mesh refinement, confirming the convergence of the current procedure for estimating the curvature.

3.3.2. Case of a surface parabolic in x and y. Consider the case of the surface defined over the octant $x, y, z \in [0, 1]$ by the relation $z = 16x(x-1)y(y-1)$. Comparison between the analytical and numerical curvatures indicates a large disparity in error. The error is found to be much larger along the edges, especially around the corners, compared to the core region. The mesh is not optimized along the edges. Although the mesh chosen is relatively fine, the discretized surface does not adhere well along the edges. As in the case of the sphere, all nodes coincide with the analytically prescribed surface, but the deviation between the element centroids and the surface can exceed 40% in the corner regions. The normal vectors to these elements are thus inaccurately estimated. Consequently, the estimation of the curvature, which is based on that of the normal vectors, is expected to be inaccurate in the corner region.

Generally, the rate of convergence with mesh refinement is good as Table II indicates. Four meshes are used, which consist of 100, 400, 900 and 2500 elements. Each mesh is constructed on the basis of the imposed number of nodes along the x- and y-axis. The relative error varies from 0.524 for the coarsest mesh to 0.046 for the finest, and the standard deviation varies from 1.910 to 0.044.

In conclusion, the proposed scheme for the estimation of the curvature depends strongly on the mesh of the discretized surface. The major influencing factors that lead to a good estimate are: the mesh size, the mesh regularity and a good estimate of the normal vectors to the elements.

3.4. Contact between free surface and confining wall(s)

Initially, the fluid is assumed to occupy a prescribed volume, Ω_0, which is taken as the starting step for the computation. Typically, Ω_0 is bounded by the wetted boundary, $\Gamma_w(0)$, and the

free surface, $\Gamma_f(0)$. In this work, it is assumed that any part of the fluid in contact, or coming in contact during the flow with the cavity walls, adheres subsequently to the walls. The line of contact between free surface and rigid boundaries is assumed to remain stationary.

The cavity walls are discretized into an appropriate number of elements that serve only to confine the fluid but do not come into the flow calculation. The number of cavity elements can thus be arbitrarily large, leading to an accurate representation of the cavity shape. This is particularly advantageous for practical situations where the geometry is typically complex. Obviously, the mesh density of the wetted boundary need not match that of the surrounding cavity. In other words, the accuracy in cavity representation is usually far superior to that of the surface bounding the moving fluid. A node or element that comes in contact with the wall is assumed to subsequently adhere to it. Contact is assumed to be established once the fluid has come close to the cavity wall to within a certain distance, which is usually taken to be of the order of an element size.

The boundary conditions imposed at a given element depend on whether the element belongs to the free surface or the cavity. As mentioned above, initially, the domain boundary consists of a free surface and a wetted surface. At the free surface, conditions (6) and (7) apply. The flow velocity is entirely specified at the wetted surface. These boundary conditions remain applicable as the flow evolves during the early stages, until the free surface comes in contact with the surrounding cavity wall. At the contact region, which may be simply or multiply connected, the boundary conditions change from those on a free surface to stick conditions at the wall.

The issue of boundary conditions at the contact line between the free surface and rigid wall is an open one. From a modelling point of view, three types of contact condition are commonly adopted in the region where the deforming free surface comes into contact with the solid wall. Contact between the free surface and the wall is a curve in space for three-dimensional flow, and a point for two-dimensional flow. The contact conditions are fixed contact line (point) condition (stick condition), fixed contact angle condition (slip condition), or mixed condition involving both fixed line (point) and angle. In general, the fixed contact line condition is suitable for static contact lines whereas the contact angle condition is predominantly used for moving or dynamic contact lines. Although the unsteady nature of the flow field is better accounted for using the contact angle condition, the fixed contact line condition is adopted in the current study due to the quasi-steady assumption. More precisely, the fluids considered here are assumed to be highly viscous, and the stick condition is likely to hold. Furthermore, the current method can easily accommodate other conditions where the contact line is allowed to move in a constrained or unconstrained manner. In general the specification of a contact angle is not obvious, especially under dynamic conditions, as no theory allows its prediction. The angle is often prescribed based on experimental measurement. Please refer to the review by Floryan and Rasmussen [8] for further discussion.

4. DISCUSSION AND RESULTS

The formulation and solution procedure are now applied for three-dimensional complex flow configurations of the moving boundary type, with emphasis on transient mixing problems. In particular, the flow of a fluid initially occupying a cubic, rectangular, and a cylindrical domain will be examined. Surface tension effects will be explored in the latter configuration. All prob-

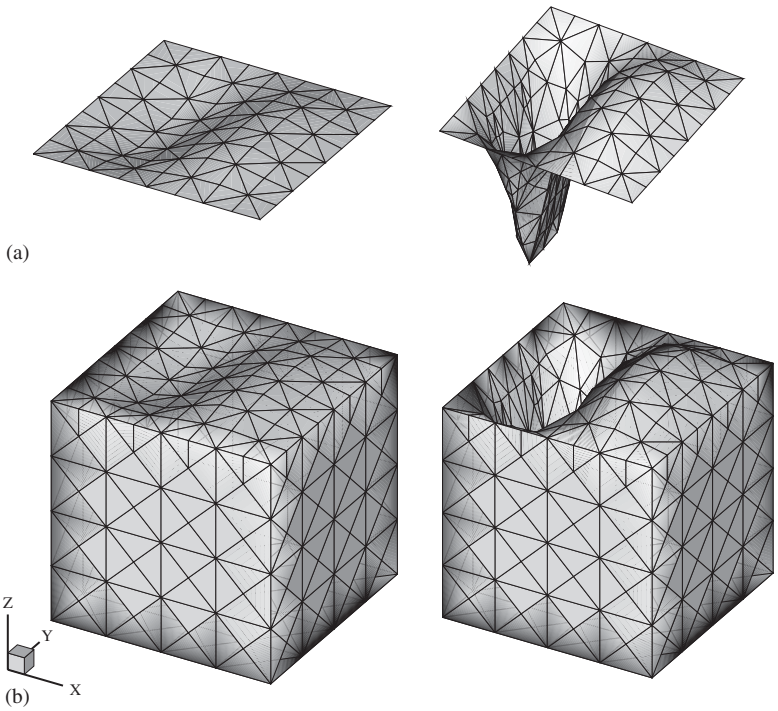

Figure 3. Transient free-surface flow with initial square domain shown in the initial and late stages at $t = 1$ and 8, respectively. The figure shows the free surface alone (a), and the full perspective (b). The set of axes are shown detached for clarity.

lems will be discussed in the Cartesian (x, y, z) space, with (u, v, w) being the corresponding velocity vector components. The results are reported in terms of dimensionless quantities.

4.1. Flow of a fluid initially occupying a cubic domain

Consider first the flow inside a partially filled cavity of square base of unit side (similarly to Figure 1). The fluid is assumed to occupy initially the cubic domain $(x, y, z) \in [0, 1] \times [0, 1] \times [0, 1]$. The flow is induced by the translation of the lid at $z = 0$. The flow is thus the transient counterpart of typical steady lid-driven cavity flow. The flow is examined assuming that the lower lid, spanning the (x, y) plane, moves at constant velocity in the x direction of unit value. Surface-tension effect is neglected for this configuration. The fluid is assumed to be initially at rest.

Figure 3 shows the location and shape of the free surface at an early stage ($t = 3$), and a relatively late stage ($t = 12$). The free surface alone is shown in Figure 3(a), and a full perspective is shown in Figure 3(b). Note that the flow is symmetric with respect to plane $y = 0.5$. Given their geometrical simplicity, the walls of the cavity need not be discretized in this case; they serve only (together with the free surface) as limits to the flow domain. As the fluid deforms, mesh elements are added (removed) in regions of extension (compression), including regions in the wall planes. The fluid is assumed to fully adhere to the walls, includ-

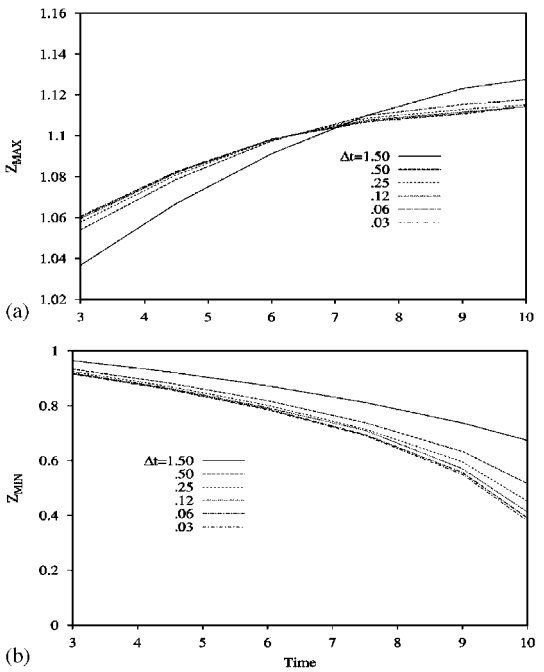

Figure 4. Evolution of the maximum (a) and minimum (b) height for a fluid initially occupying a cubic domain. The figure shows the influence of the time increment.

ing the contact lines. Figure 3 clearly indicates that despite the linearity of the (inertialess) fluid, the flow response is non-linear with time. Indeed, a closer quantitative assessment is inferred from Figure 4, where the evolution of the maximum height, $z_{\max}$, and the minimum height, $z_{\min}$, are plotted in Figures 4(a) and 4(b), respectively. In order to assess the convergence of the time-stepping scheme, several time increments are used, ranging from 0.3 to 1.5 time units. The relatively large magnitude of the time increment, Δt, is an indication of the low rate of flow and surface deformation. Both figures indicate the relatively slow rate of surface movement in the early stages, eventually displaying a fast rate of growth (decay) for the maximum (minimum) surface elevation. Convergence is essentially attained for $\Delta t < 0.12$.

A detailed account of the flow is obtained upon examining the flow field and free surface movement in the (symmetric) section $y = 0.5$, as shown in Figure 5. The figure displays the streamlines (Figure 5(a)), the contours of the axial velocity, u, (Figure 5(b)) and vertical velocity, w, (Figure 5(c)). The flow field in Figure 5(a) points to little change in flow structure as a result of the surface deformation, except in the region just below the free surface. The field structure is essentially unaffected by the cutting of the free surface, except perhaps that the flow gradient is diminished somewhat in the left-hand region in the later stage. A more accurate assessment is obtained from Figures 5(b) and 5(c). Figure 5(b) indicates that the depression in the free surface has caused the axial flow to weaken, or vanish, over a deeper region below the free surface. There is a drop in the reverse flow in the regions surrounding the

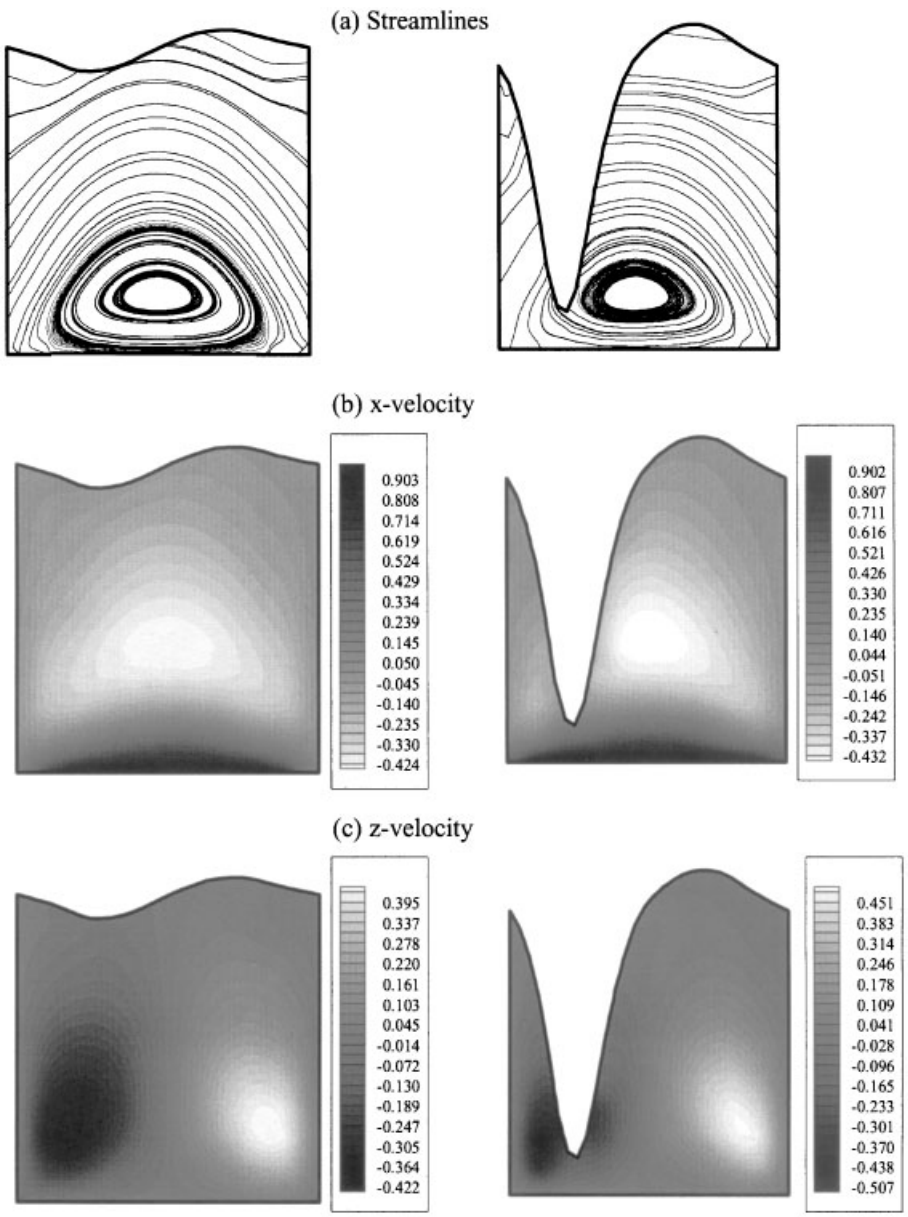

Figure 5. Flow field in the cross-section plane $y = 0.5$ at $t = 3$ and 12 for a fluid initially occupying a cubic domain. The figure shows the velocity field (a), contours of the x-velocity, u, (b) and z-velocity, w (c) components.

depression. However, there is some axial flow intensification in the lower left-hand corner. The vertical flow also diminishes below the free surface (Figure 5(c)). There is an intensification of vertical flow in the lower corner regions.

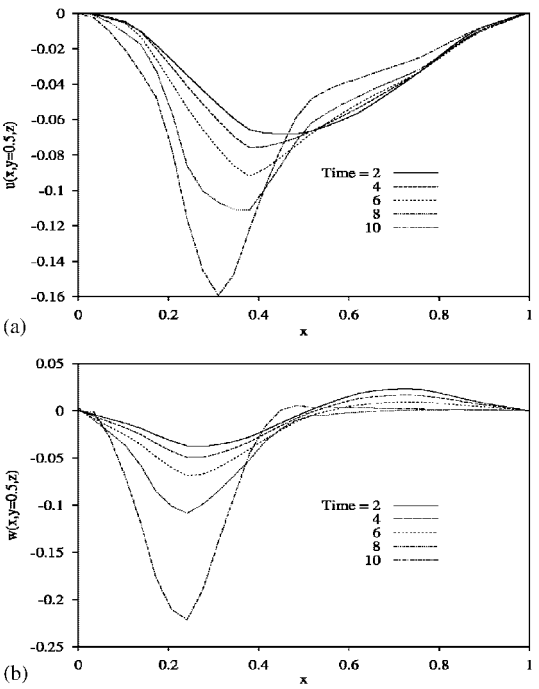

Figure 6. Velocity distributions along the x direction at the free surface in the section plane $y = 0.5$ at various stages, for a fluid initially occupying a cubic domain. The figure shows (a) the x- and (b) z-velocity components.

The velocity field at the free surface is further appreciated from Figure 6. The distributions of u and w at the free surface in the mid-section ($y = 0.5$) are plotted along x in Figures 6(a) and 6(b), respectively. Both velocity components exhibit a minimum at any stage, which strengthens with time (with surface deformation). While the minimum in w tends to remain localized (at around 0.23), the minimum in u tends to shift toward the wall $x = 0$, but remains upstream of the location of the w minimum. The figures indicate that the axial and vertical flows are of the same order of magnitude at any time (at least in this section, $y = 0.5$). The axial flow remains negative, indicating a direction to the left of the flow, in the (x,z) plane. Although the downward flow is predominant, there is a relatively weak upward flow for $x > 0.4$ that weakens with surface deformation, and eventually levels off with time.

The overall flow at the free surface is shown in Figure 7 at the two stages $t = 3$ and 12. The contours of surface elevation (Figure 7(a)), w (Figure 7(b)), u (Figure 7(c)), and v (Figure 7(d)) are displayed. It is interesting to observe that the contours of surface elevation do not uniformly correspond to those of the vertical velocity. This is particularly the case at $t = 12$. The discrepancy originates from the small non-uniformity of the vertical flow in the depressed region of the free surface. A similar pattern is exhibited by the u contours (Figure 7(c)). There is essentially no axial flow in the upper free surface region relatively to the depressed region, especially at the later stage. In this case, the flow is stronger in the positive direction near the plane $x = 0$, which is not at all evident from Figure 6(a). Indeed,

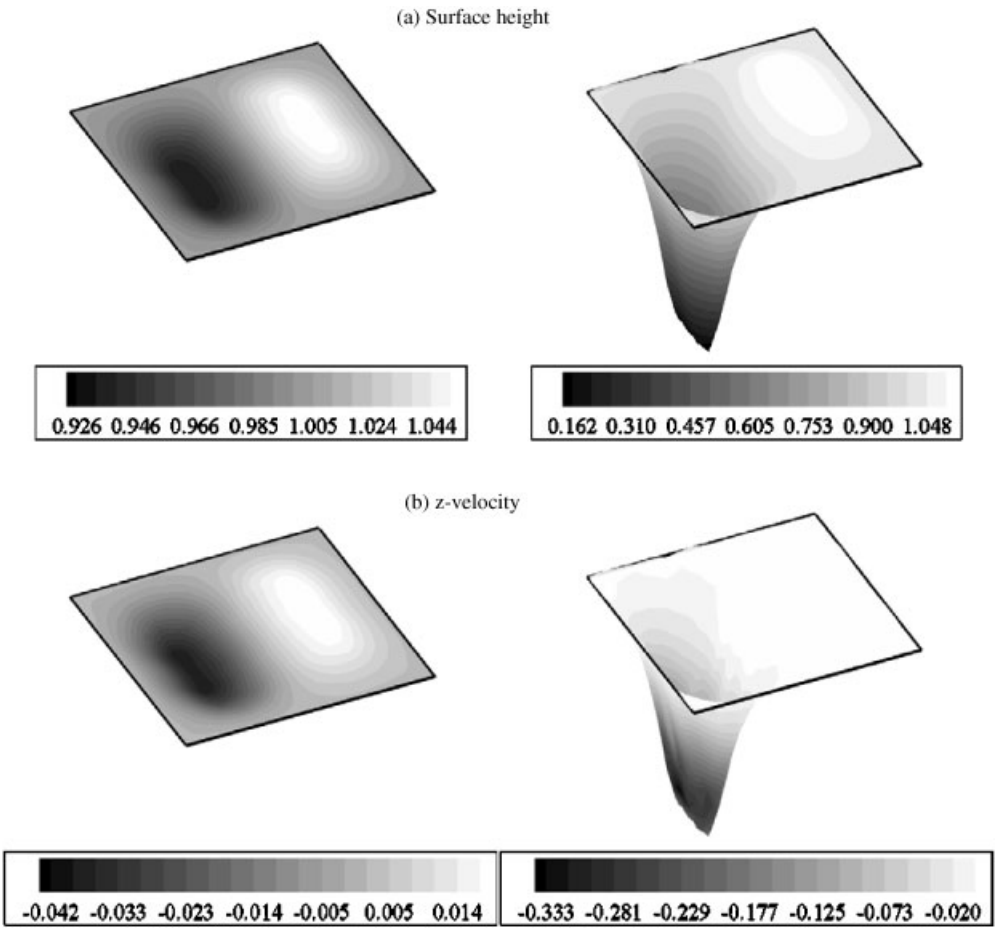

Figure 7. Flow field over the free surface, for a fluid initially occupying a cubic domain. The figure shows the contours of the surface height (a), the z-velocity (b) x-velocity (c) and y-velocity (d) components.

this flow accelerates near the tip of the free surface depression. Finally, Figure 7(d) indicates that the transverse flow is one order of magnitude weaker initially, but becomes increasingly stronger with surface deformation, particularly near the tip of the depression.

4.2. Flow of a fluid initially occupying a rectangular domain

Consider now the flow of a fluid occupying initially a three-dimensional rectangular domain with height equal to twice the side of the square base, i.e. $(x, y, z) \in [0,1] \times [0,1] \times [0,2]$. Figure 8 shows the location and shape of the free surface at an early stage ($t = 200$), and a relatively late stage ($t = 1700$). The flow is again symmetric with respect to the plane $y = 0.5$. The remarkable feature of this flow, compared to that in Figure 3, is that in this case the flow responds with a time scale that is roughly 100 times slower than in the case of a fluid

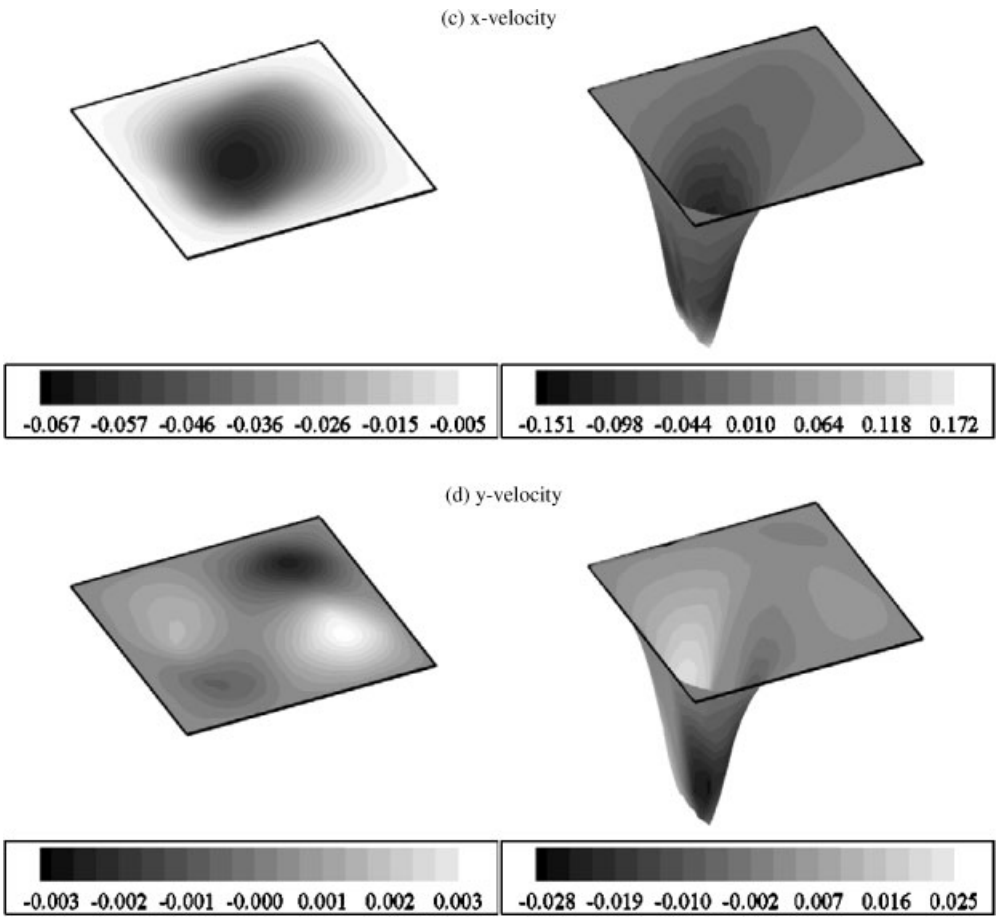

Figure 7. *Continued.*

occupying initially a cubic domain. Indeed, a closer quantitative assessment is inferred from Figure 9, where the maximum elevation, $z_{\max}$, and the minimum elevation, $z_{\min}$, of the free surface are plotted against time. The rate of flow and surface deformation is exceedingly slow, particularly in the early stage. The figure indicates the relatively slow rate of surface movement in the early and late stages, in contrast to the sharp drop displayed in Figure 4. Note that the rate of change in surface extrema is essentially linear in the late stages. More importantly, this rate is slow as a result of the emergence of two flow sub-domains that are typical of flows in cavities of large aspect ratio (see next).

The flow field and free surface shape in the section plane $y = 0.5$ are shown in Figure 10. The figure displays the streamlines (Figure 10(a)), and the contours of the axial velocity, u, (Figure 10(b)) and vertical velocity, w, (Figure 10(c)). The flow field in Figure 10(a) points to essentially no change in flow structure as a result of the surface deformation near the bottom base. Near the free surface, however, the vortical flow just below the free surface tends to

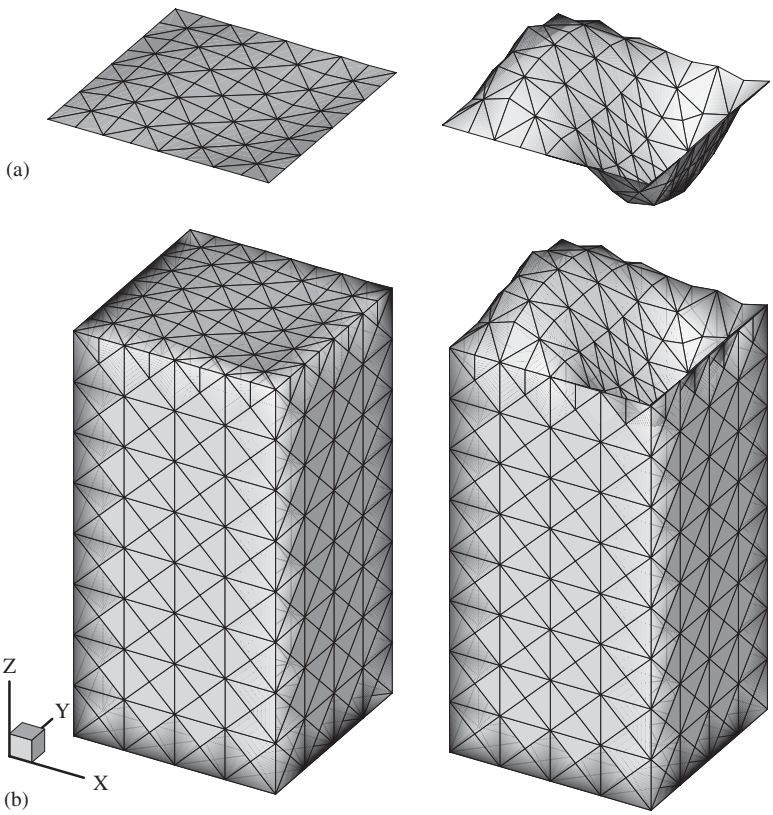

Figure 8. Transient free-surface flow of a fluid occupying initially a rectangular domain shown in the initial and late stages at $t = 200$ and 1700, respectively. The figure shows the free surface alone (a), and the full perspective (b). The set of axes are shown detached for clarity.

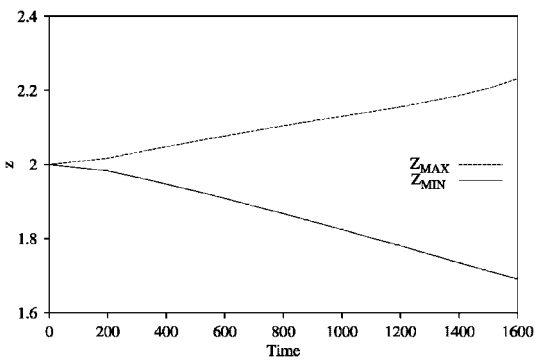

Figure 9. Evolution of the maximum and minimum heights for a fluid initially occupying a rectangular domain.

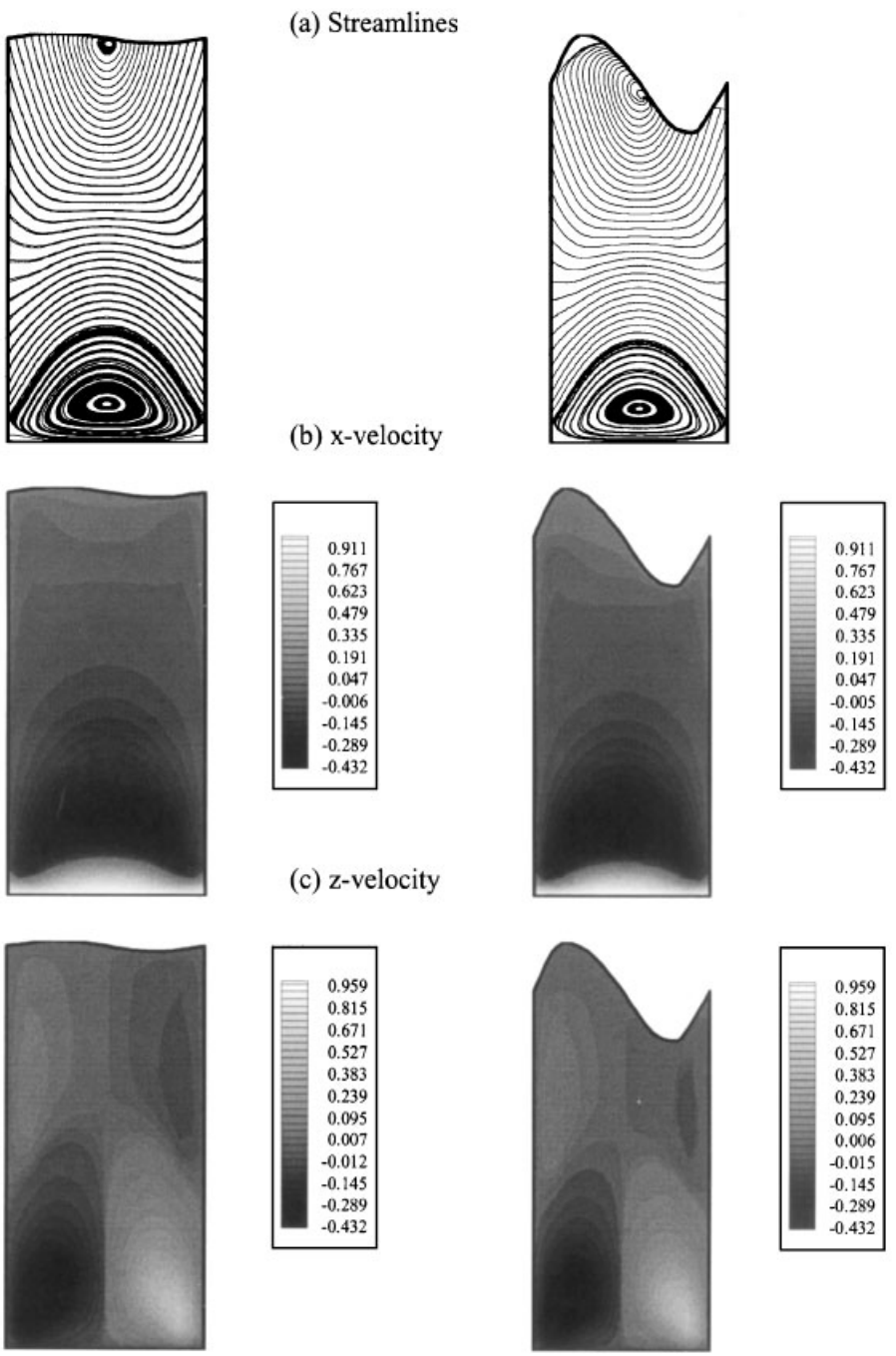

Figure 10. Flow field in the cross-section plane $y = 0.5$ at $t = 200$ and 1700 for a fluid initially occupying a rectangular domain. The figure shows the streamlines (a), contours of the x-velocity (b) and z-velocity (c) components.

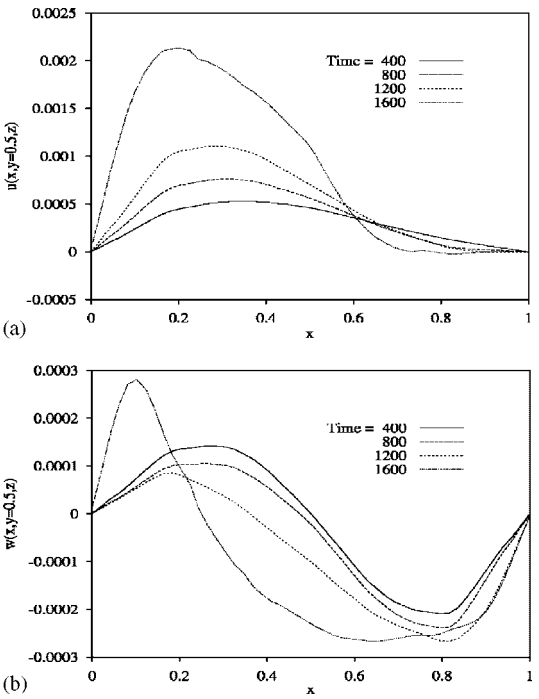

Figure 11. Velocity distributions along the x direction at the free surface in the section plane $y = 0.5$ at various stages, for a fluid initially occupying a rectangular domain. The figure shows (a) the x- and (b) z-velocity components.

develop toward that encountered in lid-driven cavity flow with no free surface (rigid upper lid). Figure 10(b) indicates that the depression in the free surface has caused the axial flow to weaken, or vanish, over a deeper region below the free surface. There is a drop in the reverse flow in the regions surrounding the depression. The downward flow strengthens just below the free surface in the upper right-hand corner (Figure 10(c)). There is an intensification of vertical flow also in the upper left-hand corner. The evolution of u and w at the free surface are plotted along x in Figures 11(a) and 11(b), respectively. Figure 11(a) indicates the dominance of a rightward flow that strengthens with free surface deformation. This is in sharp contrast with Figure 6(a), where the axial flow is clearly to the left. The vertical flow is overall antisymmetric with respect to $x = 0.5$, but somewhat less in the relatively later stages of flow. This is again in contrast to the previous flow where w becomes quickly asymmetric with respect to $x = 0.5$ (Figure 6(b)). It is interesting to observe that the minimum in the axial flow occurs slightly to the right of the depression, where the minimum in the vertical flow occurs.

The overall flow at the free surface is shown in Figure 12 at the two stages $t = 200$ and 1700. The contours of surface elevation (Figure 12(a)), velocity components w (Figure 12(b)), u (Figure 12(c)), and v (Figure 12(d)) are displayed. It is clear from Figures 12(a) and 12(b) that the location maximum (minimum) surface elevation does not correspond to maximum

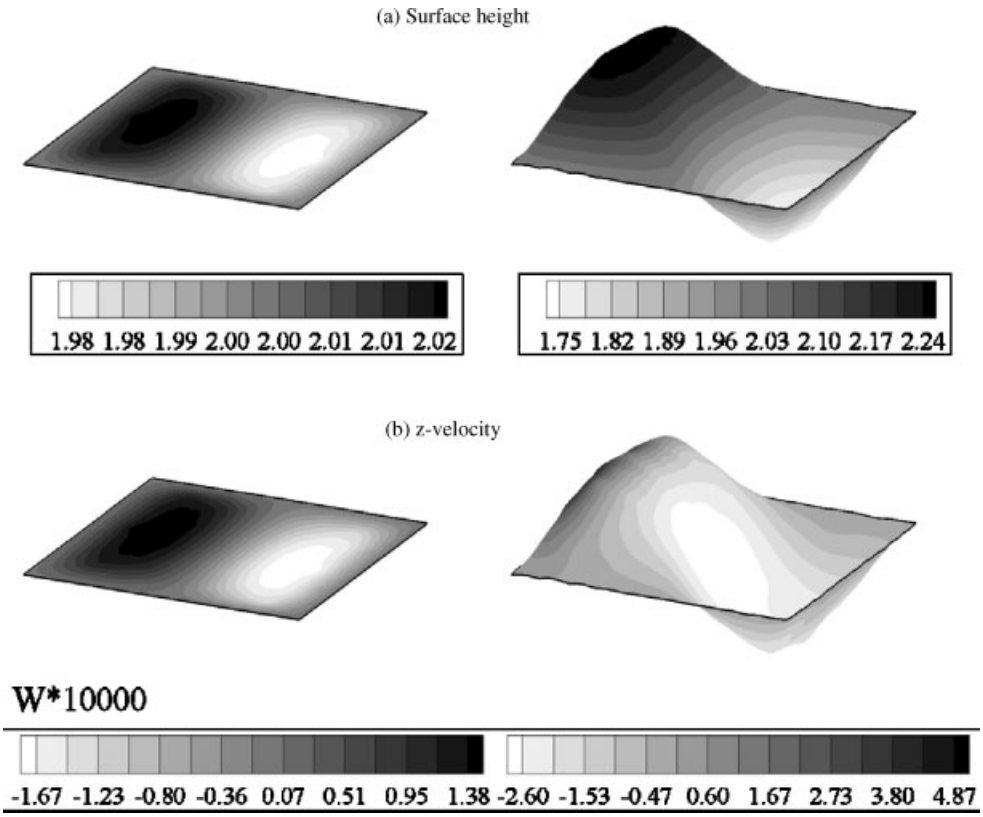

Figure 12. Flow field over the free surface, for a fluid initially occupying a rectangular domain. The figure shows the contours of the surface height (a), the z-velocity (b) x-velocity (c) and y-velocity (d) components.

(minimum) vertical velocity. This is particularly evident at $t = 1700$. In contrast, the u contours in Figure 12(c) indicates the culmination of axial flow at the maximum of surface elevation. The axial flow is entirely in the positive direction at the free surface. Finally, Figure 12(d) indicates that the transverse flow is one order of magnitude weaker initially, but becomes increasingly stronger with surface deformation, particularly near the free surface maximum (see in contrast Figure 6(d)).

4.3. Flow of a fluid initially occupying a cylindrical domain

Consider finally the flow inside a long cylinder with base of unit diameter. The fluid is assumed to occupy initially the cylindrical domain of unit height. The flow is examined assuming that the lower lid, spanning the unit circle in the (x, y) plane, moves at constant velocity in the x direction of unit value. Surface-tension effect is neglected at first for this configuration, but it will be examined in some detail shortly. The fluid is assumed to be initially at rest.

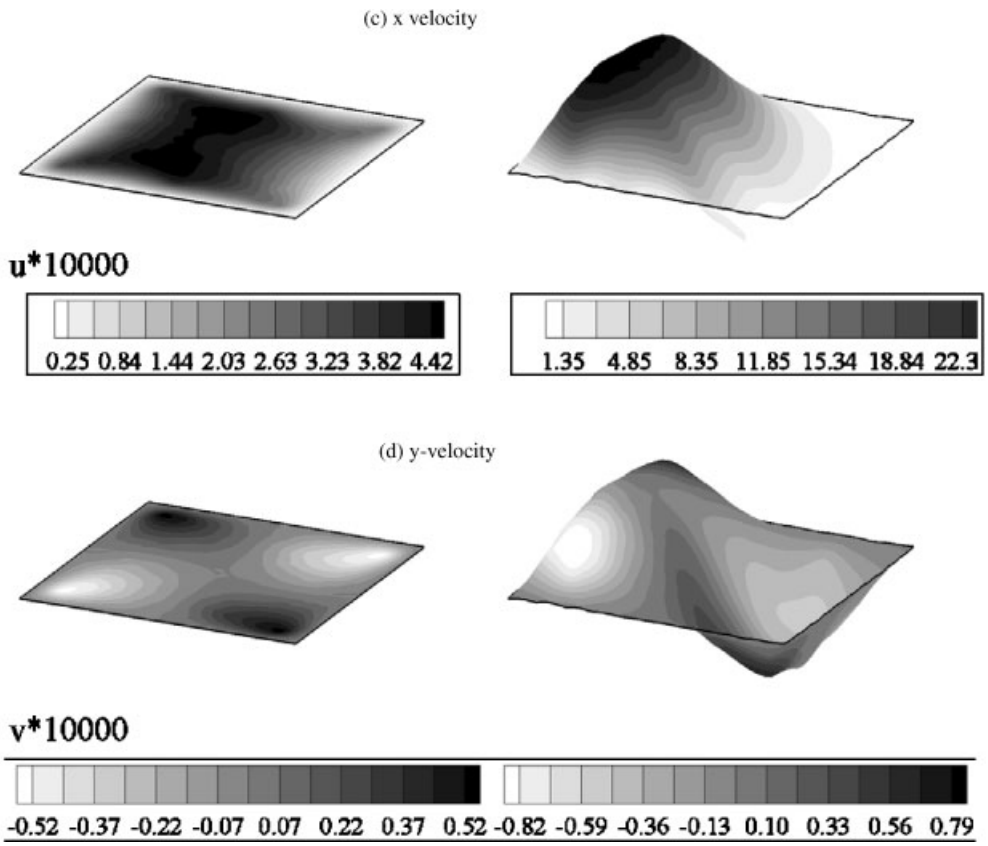

Figure 12. *Continued.*

Similarly to Figure 3, Figure 13 shows the location and shape of the free surface at an early stage ($t = 8$), and a relatively late stage ($t = 16$). The free surface alone is shown in Figure 13(a), and a full perspective is shown in Figure 13(b). The flow is again symmetric with respect to the plane $y = 0.5$. Note that, unlike the flow inside a rectangular domain, the time scale for the problem is of the same order of magnitude as the flow in a cubic domain. The non-linear character of the flow is illustrated in Figure 14, where the evolution of the maximum elevation, $z_{\max}$, and the minimum elevation, $z_{\min}$, of the free surface are plotted. Both curves indicate the relatively slow rate of surface movement in the early stages, eventually displaying a fast rate of growth (decay) for the maximum (minimum) height. However, the rate of change in $z_{\min}$ is higher than that in $z_{\max}$.

A detailed account of the flow is obtained upon examining the flow field and free-surface movement in the (symmetric) section $y = 0.5$, as shown in Figure 15. The figure displays the streamlines (Figure 15(a)), axial velocity contours (Figure 15(b)), and vertical velocity contours (Figure 15(c)). The flow field in Figure 15(a) points to a more significant change in flow structure with surface deformation than in the case of the cubic configuration (Figure 5) as a result of curvature effect from the cylinder wall. The field structure indi-

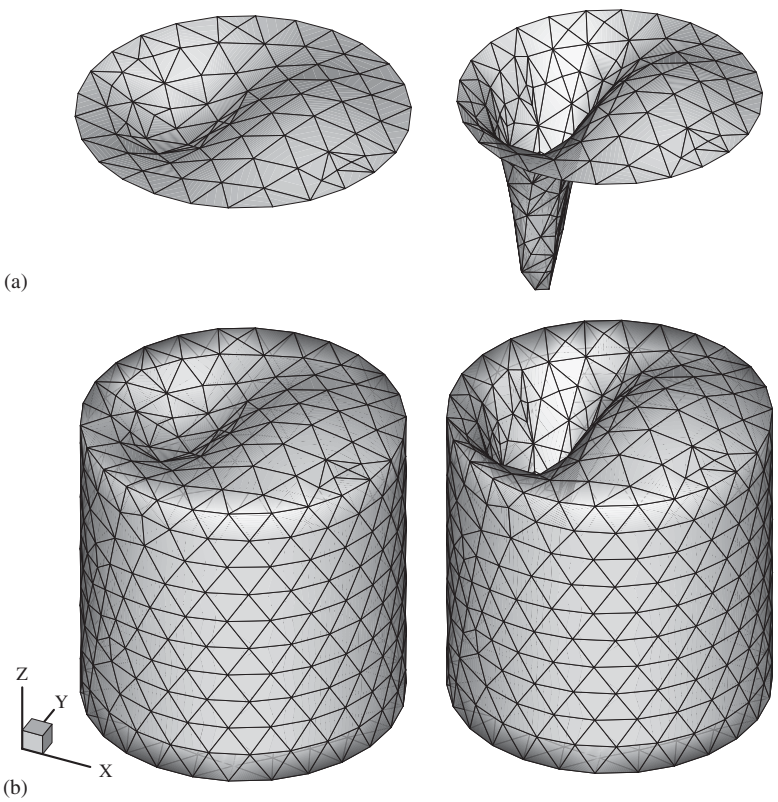

Figure 13. Transient free-surface flow of a fluid occupying initially a cylindrical domain shown in the initial and late stages at $t = 8$ and 16, respectively. The figure shows the free surface alone (a), and the full perspective (b). The set of axes are shown detached for clarity.

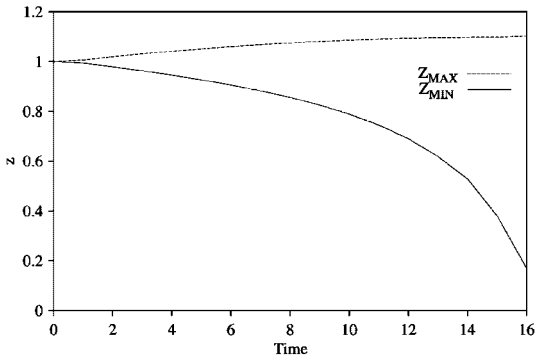

Figure 14. Evolution of the maximum and minimum heights for a fluid initially occupying a cylindrical domain.

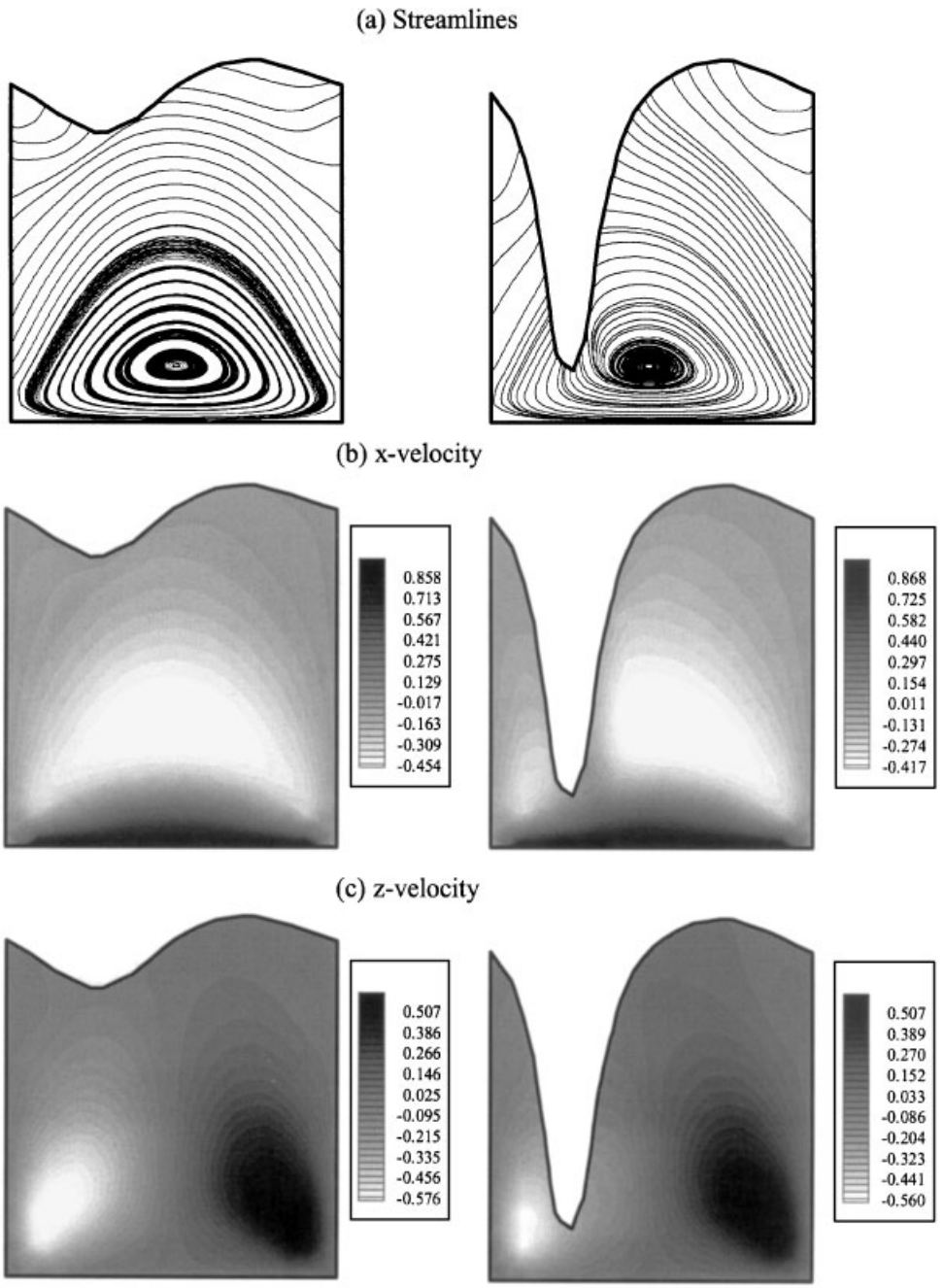

Figure 15. Flow field in the cross-section plane $y = 0.5$ at $t = 8$ and 16 for a fluid initially occupying a cylindrical domain. The figure shows the streamlines (a), contours of the x-velocity (b) and z-velocity (c) components.

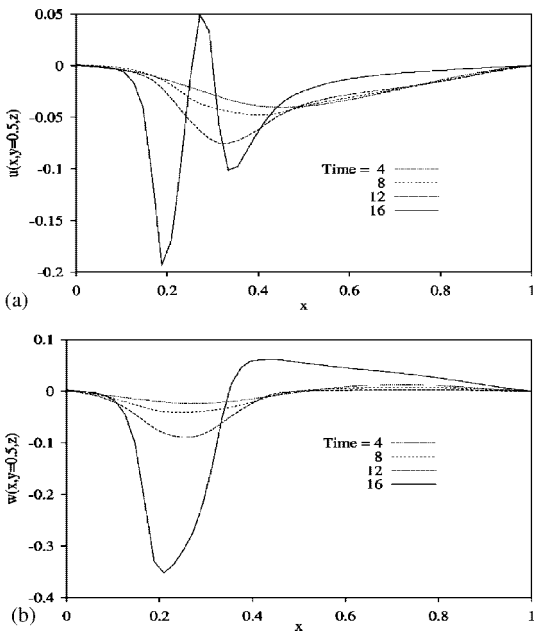

Figure 16. Velocity distributions along the x direction at the free surface in the section plane $y = 0.5$ at various stages, for a fluid initially occupying a cylindrical domain. The figure shows (a) the x- and (b) z-velocity components.

cates a strengthening of the vertical flow due to the cutting of the free-surface, especially in the upper right-hand region. A more accurate assessment is obtained from Figures 15(b) and 15(c). Figure 15(b) indicates that the depression in the free-surface has caused the axial flow to weaken, or vanish, especially just below the free surface and deeper. There is a drop in the reverse flow in the regions surrounding the depression. However, there is some axial flow intensification in the lower right-hand corner and just below the lower free-surface tip. The vertical flow also diminishes below the free surface (Figure 15(c)). However, there is an intensification of vertical flow in the upper left-hand corner, confirming what is observed in Figure 15(a).

The velocity field at the free surface is further appreciated from Figure 16. The distributions of u and w at the free surface in the midsection ($y = 0.5$) are plotted along x in Figures 16(a) and 16(b), respectively. Both velocity components exhibit a minimum at any stage, which strengthens with time (with surface deformation). The situation is similar to that depicted from Figure 6, except that in the present case, both velocity components display a maximum in the later stage of surface deformation, indicating a relatively abrupt surge in upward flow near $x = 0.4$. While the minimum in w tends to remain localized (at around 0.23), the minimum in u tends to shift toward the wall $x = 0$, but remains upstream of the location of the w minimum. The figures indicate that the axial and vertical flows are of the same order of magnitude at any time (at least in this section, $y = 0.5$). The axial flow remains overall negative, indicating a direction to the left of the flow, in the (x, z) plane, except at

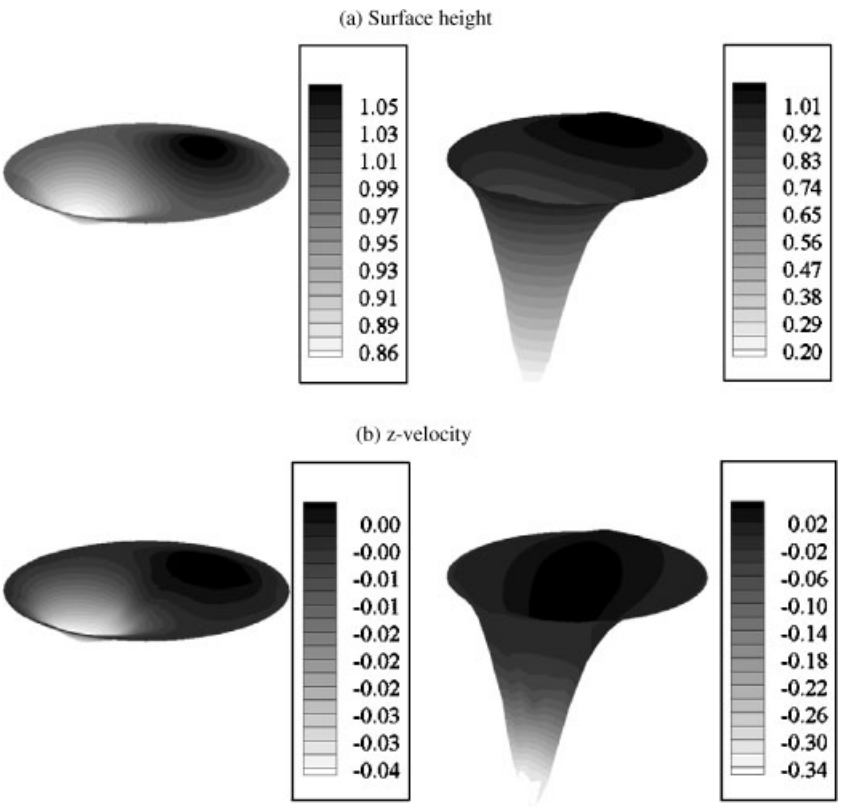

Figure 17. Flow field over the free surface, for a fluid initially occupying a cylindrical domain. The figure shows the contours of the surface height (a), the z-velocity (b) x-velocity (c) and y-velocity (d) components.

$t = 16$ when there is some axial movement to the right that is not evident from Figure 15(b). Although the downward flow is predominant, there is a relatively weak upward flow for $x > 0.4$, which in contrast to the cubic flow tends to strengthen with surface deformation (see Figure 6(b)).

The overall flow at the free surface is shown in Figure 17 at the two stages $t = 8$ and 16. The contours of surface elevation (Figure 17(a)), w (Figure 17(b)), u (Figure 17(c)), and v (Figure 17(d)) are displayed. Figures 17(a) and 17(b) indicate that most of the vertical movement of the free surface occurs along the depressed region, particularly at the later stages. This is not exactly the case as far as the axial movement is concerned (Figure 17(c)). There seems to be a non-vanishing extensional gradient in the upper region of the free surface, which is stronger than in the case of cubic flow (Figure 7(c)). In contrast to the flow in Figure 7(c), the axial flow is dominantly positive. The transverse flow is overall weak as observed from Figure 17(d), but remains of the same strength as the axial flow. This is in sharp contrast with the cubic flow where the transverse flow is one order of magnitude

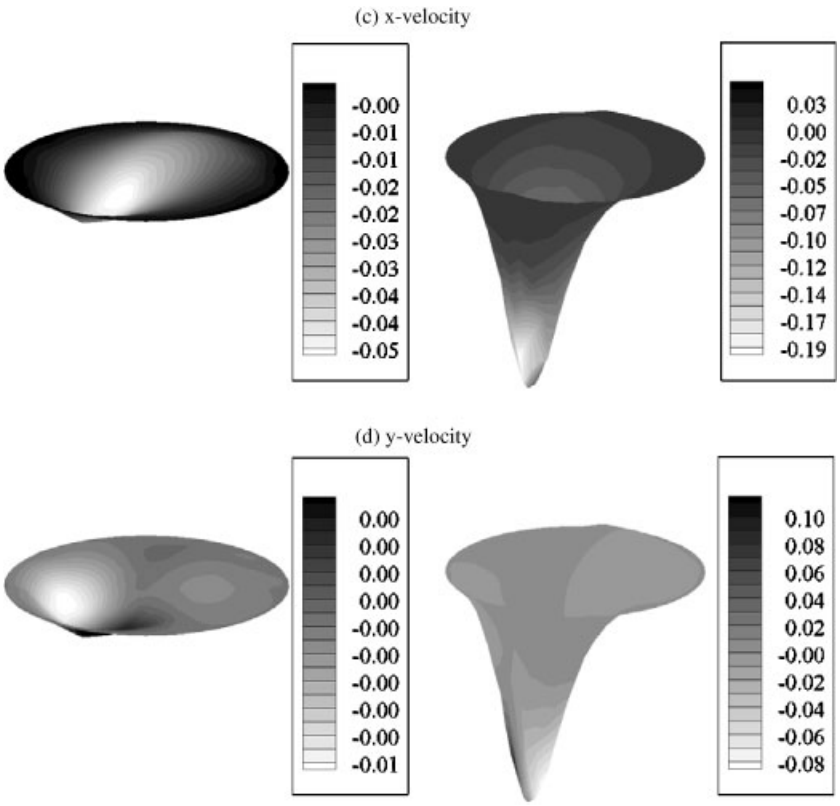

Figure 17. *Continued.*

smaller than the axial flow (see Figure 7(d)). It is interesting to observe from Figure 17(d) that most of the flow activity in the transverse is concentrated in the bottom region of the free surface.

Finally, the effect of surface tension will be examined, which has been neglected so far. It is found, and as expected, that surface tension does not bring about significantly different qualitative behaviour. Figure 18 shows the evolution of the maximum and minimum free surface elevations for various values of the capillary number, Ca. The curves corresponding to the absence of surface tension ($\mathrm{Ca} \to \infty$) have of course been reported earlier but they are included here for reference. In general, surface tension tends to prohibit deformation. The figure indicates that the influence of surface tension is linear with surface deformation.

5. CONCLUSION

The simulation of three-dimensional transient free-surface lid-driven flow inside cavities of arbitrary shape is carried out for Stokes flow. An adaptive Lagrangian three-dimensional boundary-element approach is proposed. The mesh refinement algorithm is simple and yet

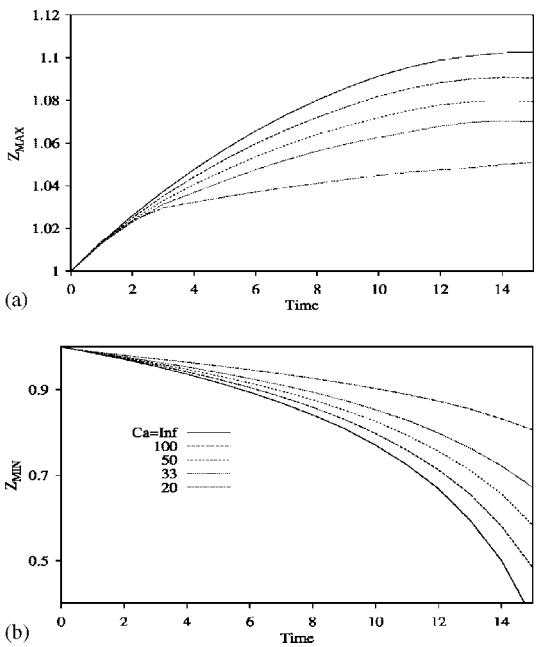

Figure 18. Influence of surface tension on surface deformation for the cylindrical flow. The figure shows the influence of the capillary number on the evolution of the maximum and minimum surface elevation.

is found to be robust and suitable for moving-free surface flow. Three flow configurations are examined, namely when the fluid occupies initially a cubic, a rectangular and a cylindrical domain. These flows are evidently of close relevance to mixing. The free surface typically exhibits a depression resulting from the vortical flow in the core of the cavity. For the cubic and cylindrical flows, the free surface deforms indefinitely, until the depressed region reaches the bottom of the cavity. Deformation accelerates with time. For a fluid occupying initially the cavity with 2:1 aspect ratio, surface deformation is retarded considerably, and the shape of the free surface reaches essentially steady state.

ACKNOWLEDGEMENTS

This work is supported by the Natural Sciences and Engineering Research Council of Canada.

REFERENCES

1. Iwatsu R, Ishi K, Kawamura TK, Hyun JM. Simulation of transition to turbulence in a cubic cavity. *AIAA Paper*, vol. 89, 1989; 40.1.
2. Deshipnde MD, Shankar PN. Direct numerical simulation of a complex turbulent flow. *Current Science* 1994; **66**:767.
3. Tran-cong T, Blake JR. General solution of the Sokes' flow equations. *Journal of Mathematical Analysis and Applications* 1982; **90**:72.
4. Verstappen RW, Veldman AE. Direct numerical simulation of a 3D turbulent flow in a cavity. In *Computational Fluid Dynamics* '94, Wagner E. *et al.* (eds). Wiley: New York, 1994.

5. Zhang Y, Street RL, Doeff J. A non-staggered grid, fractional step method for time-dependent incompressible Navier–Stokes equations in curvilinear coordinates. *Journal of Computational Physics* 1994; **114**:18.
6. Shankar PN. Three-dimensional eddy structure in a cylindrical container. *Journal of Fluid Mechanics* 1997; **342**:97.
7. Shankar PN. Three-dimensional flow in a cylindrical container. *Physics of Fluids* 1998; **10**:540.
8. Floryan JM, Rasmussen H. Numerical methods for viscous flows with moving boundaries. *Applied Mechanics Reviews* 1989; **42**:323.
9. Nickell RE, Tanner RI, Caswell B. The solution of viscous incompressible jet and free-surface flows using finite element method. *Journal of Fluid Mechanics* 1974; **65**:189.
10. Siliman WJ, Scriven LE. Separating flow near a static contact line: slip at a wall and shape of a free surface. *Journal of Computational Physics* 1980; **34**:287.
11. Ruschak KJ. A method of incorporating free boundaries with surface tension in finite element fluid flow simulation. *International Journal for Numerical Methods in Engineering* 1980; **15**:639.
12. Kawahara M, Miwa T. Finite element analysis of wave motion. *International Journal for Numerical Methods in Engineering* 1984; **20**:1193.
13. Bach P, Hassager O. An algorithm for the use of the Lagrangian specification in Newtonian fluid mechanics and applications to free surface flows. *Journal of Fluid Mechanics* 1985; **152**:173.
14. Ramaswany B, Kawahara M. Lagrangian finite element analysis applied to viscous free surface fluid flow. *International Journal for Numerical Methods in Fluids* 1987; **7**:953.
15. Chipada S, Jue TC, Joo SW, Wheeler MF, Ramaswamy R. Numerical simulation of free-boundary problems. *Computers and Fluid Dynamics* 1996; **7**:91.
16. Khayat RE, Luciani A, Utracki LA. Boundary-element analysis of planar drop deformation in confined flow. Part I. Newtonian fluids. *Engineering Analysis with Boundary Elements* 1997; **19**:279.
17. Khayat RE, Huneault M, Utracki LA, Duquette R. A boundary element analysis of planar drop deformation in the screw channel of a mixing extruder. *Engineering Analysis with Boundary Elements* 1998; **21**:155.
18. Khayat RE. Boundary-element analysis of planar drop deformation in confined flow. Part II. Viscelastic fluids. *Engineering Analysis with Boundary Elements* 1998; **22**:291.
19. Khayat RE. A boundary-only approach to the deformation of a shear-thinning drop in extensional Newtonian flow. *International Journal for Numerical Methods in Fluids* 2000; **33**:559.
20. Khayat RE. Three-dimensional boundary-element analysis of drop deformation for Newtonian and viscoelastic systems. *International Journal for Numerical Methods in Fluids* 2000; **34**:241.
21. Khayat RE, Luciani A, Utracki LA, Godbille F, Picot J. Influence of shearing and elongation on the deformation of drops in a convergent/divergent tube of Newtonian and viscoelastic fluids. *International Journal of Multiphase Flow* 2000; **26**:17.
22. Khayat RE, Derdouri A, Hebert LP. A boundary-element approach to three-dimensional gas-assisted injection molding. *Journal of Non-Newtonian Fluid Mechanics* 1995; **57**:253.
23. Khayat RE, Elsin W, Kim K. An adaptive boundary-element approach to 2D moving-boundary flow of viscous fluids. *International Journal for Numerical Methods in Fluids* 2000; **33**:847.
24. Khayat RE, Raducanu P. A coupled finite element/boundary element approach for the three-dimensional simulation of air venting in blow molding and thermoforming. *International Journal for Numerical Methods in Engineering* 1998; **43**:151.
25. Khayat RE, Derdouri A, Frayce D. Boundary-element analysis of three-dimensional transient mixing processes of Newtonian and viscoelastic fluids. *International Journal for Numerical Methods in Fluids* 1998; **28**:815.
26. Khayat RE. A boundary-element analysis of 3D multiply-connected cavity mixing of polymer solutions. *International Journal for Numerical Methods in Fluids* 1999; **31**:1173.
27. Peraire M, Vahdati K, Morgan K, Zienkiewicz OC. Adaptive remeshing for compressive flow computation. *Journal of Computational Physics* 1987; **72**:449.
28. Jin H, Wiberg NE. Two dimensional mesh generation, adaptive remeshing and refinement. *International Journal for Numerical Methods in Engineering* 1990; **29**:1501.
29. Roberti P, Melkanoff MA. Self-adaptive analysis based on stress convergence. *International Journal for Numerical Methods in Engineering* 1987; **24**:1973.
30. Rivara MC. Selective refinement/derefinement algorithms for sequences of nested triangulation. *International Journal for Numerical Methods in Engineering* 1989; **28**:2889.
31. Bachmann PL, Witchen SL, Sheppard MS, Grice KR, Yerry MA. Robust, geometrically based, automatic two-dimensional mesh generation. *International Journal for Numerical Methods in Engineering* 1987; **24**:1043.
32. Sheppard MS. Approaches to the automatic generation and control of finite element meshes. *Applied Mechanics Reviews* 1988; **41**:169.
33. Dow JO, Byrd DE. Error estimation procedure for plate bending elements. *AIAA Journal* 1990; **28**:685.
34. Batchelor GK. *Introduction to Fluid Dynamics*. Cambridge University Press, Cambridge, MA, 1967.
35. Park WC, Homsy GM. Two-phase displacement in Hele-Shaw cells: theory. *Journal of Fluid Mechanics* 1984; **139**:291.

36. Brebbia CA, Dominguez J. *Boundary Elements: An Introductory Course*. Computational Mechanics Publications and McGraw-Hill: New York, 1992.
37. Nambiar RV, Valera RS, Lawrence KL, Morgan RB, Amil D. An algorithm for adaptive refinement of triangular element meshes. *International Journal for Numerical Methods in Engineering* 1993; **36**:499.
38. Rosenberg IG, Stenger F. A lower bound on the angles of triangles constructed by bisecting the longest edge. *Mathematics of Computation* 1975; **29**:390.

